AUT Journal of Mechanical Engineering

AUT J. Mech. Eng., 10(2) (2026) 179-198
DOI: 10.22060/ajme.2025.23880.6164

Enhancing Thermo-Electrical Performance of Solid Oxide Fuel Cells through Multi-Channel Cooling System Analysis

Mohammad Taghilou*, Vahid Barati

Department of Mechanical Engineering, Faculty of Engineering, University of Zanjan, Zanjan, Iran.

ABSTRACT: Thermal stresses in solid oxide fuel cells, caused by differential expansion during thermal cycling and coefficient of thermal expansion mismatches, lead to material degradation, cracking, voltage instability, and reduced reliability, hindering commercial viability. This study introduces a novel six-channel active cooling system for solid oxide fuel cells, aimed at lowering peak temperatures, improving thermal uniformity, and stabilizing voltage output. Using three dimensional numerical simulations with hydrogen/water vapor and oxygen/nitrogen as reactants, it systematically examines how cooling parameters such as flow rate, temperature, and flow configuration affect electrochemical performance. Key results demonstrate that co-current cooling (600 K, 1×10^{-6} kg/s) reduces peak temperature by 9% (to 1387 K) but at the cost of a 133% increase in temperature non-uniformity and a 55% voltage drop due to elevated overpotentials. Conversely, counter-current cooling (1000 K, same flow rate) achieves a more balanced performance, lowering peak temperature by 6% (to 1389.11 K) while reducing non-uniformity by 21.5% and increasing output voltage by 5.5% (0.2933 V). A critical finding is that excessive cooling (1×10^{-5} kg/s) leads to premature voltage collapse, with co-current flows failing at lower current densities (e.g., 9800 A/m² at 600 K) compared to counter-current configurations. This study pioneers an active cooling optimization framework for solid oxide fuel cells, demonstrating how precisely adjusted cooling parameters balance thermal control with electrochemical efficiency.

Review History:

Received:Feb. 02, 2025
Revised: Jul. 13, 2025
Accepted: Jul. 18, 2025
Available Online: Jul. 21, 2025

Keywords:

Solid Oxide Fuel Cell
Cooling Channels
Numerical Thermal Management
Uniform Temperature Distribution
Maximum Temperature

1- Introduction

Solid oxide fuel cells (SOFCs) operate at high temperatures using porous electrodes and a solid ceramic electrolyte, offering high-power density and low emissions. However, prolonged heating/cooling cycles induce large temperature gradients, thermal stress, and cracking [1]. Thermal stress regulation requires controlling temperature variations, particularly in the positive electrode-electrolyte-negative electrode (PEN) structure [2-4]. While prior studies have explored geometric modifications of flow channels and flow arrangements to mitigate temperature non-uniformity, a critical gap remains in systematically evaluating active cooling strategies that simultaneously address peak temperature reduction, thermal uniformity, and voltage stability—key requirements for commercial SOFC durability and performance.

An effective way to reduce the temperature difference in the PEN structure is to change the geometry of the fuel and air channels. Ji et al. [5] investigated the effect of width and length of air and fuel channels, showing that reducing the height of the channel from 5 mm to 0.2 mm increases the maximum temperature difference by 40%. Danilov and Tade [6] suggested that changing the geometry of the air and fuel channel inlet can effectively reduce the temperature difference in the PEN structure. Manglik et al. [7] demonstrated that among fuel cells with rectangular, trapezoidal, and triangular channel sections, the rectangular channel exhibits the lowest temperature difference. Additionally, gas flow arrangement (co-current, counter-current, or cross-flow) significantly impacts temperature distribution in plate cells. Shen et al. [8] found that rectangular obstacles in gas flow channels slightly reduce the maximum temperature and improve hydrogen utilization in SOFCs. Kumar et al. [9] demonstrated that a trapezoidal interconnector design enhances power density by 18.2% compared to conventional rectangular designs at 1123 K. Fan et al. [10] proposed two solutions for temperature and voltage uniformity in segmented-in-series SOFCs: using a heat pipe as a fuel inlet tube and extending the downstream cell length, reducing temperature differences from 111 K to 25 K and voltage differences from 120 mV to 7 mV at 3 A. Gong et al. [11] developed a rotary L-type flow field design that enhances temperature uniformity by 40% while significantly reducing thermal gradients compared to conventional configurations. Lee et al. [12] proposed an improved interconnect design for planar SOFCs that reduces temperature variations by 34%, hydrogen molar fraction differences by 13.3%, and current density non-uniformity by 8.7% through optimized diagonal gas manifolds and channel

*Corresponding author's email: taghilou@znu.ac.ir

width adjustments.

Inui et al. [13] studied the arrangement of fuel and air flow in a planar solid oxide fuel cell with co-current and counter-current flows, indicating a lower temperature difference in the counter-current flow arrangement. Li et al. [14] showed that the location of the maximum temperature in a co-current flow occurs near the end of the fuel channel, but in counter-current flow, the maximum temperature point moves towards the fuel inlet. Sugihara and Iwai [15] studied fuel/air flow arrangements and methane-steam reforming at 770°C, showing that the maximum local temperature difference increases with higher internal modification ratios, independent of flow arrangement. However, counter-current flow (without internal modification) better reduces temperature differences. Guk et al. [16] analyzed the impact of operating temperature, fuel flow rate, and current density on temperature distribution and stability using a multi-point thermal sensor. They found that hydrogen oxidation due to fuel crossover significantly affected temperature, with electrochemical oxidation contributing to temperature gradient during loading. Kupecki et al. [17] simulated the dynamic operation of a 1000 W-class SOFC stack under fault conditions and suggested adjusting operating parameters to control temperature gradients. Kim et al. [18] conducted a three-dimensional simulation of a 1-kW SOFC stack and observed temperature differences among unit-cells and sealants near the air inlet. Xu et al. [19]te> demonstrated the achievement of a local thermal neutral state by controlling the operating potential and current density, also showing a decrease in the maximum axial temperature gradient by supplying warmer air. Jian et al. [20] established a surrogate modeling method for temperature profile reconstruction, demonstrating that accurate predictions (within 5℃ for temperature and 4℃/cm for gradients) require at least three local temperature measurements. Lin et al. [21] investigated thermal uniformity in methane-rich internal reforming SOFCs through numerical simulations, offering guidance for design and operation. Key findings include improved thermal uniformity with 5% methane fuel, a cell length-to-width ratio (Rcell) ≥ 1.0, and increased backpressure to 1.5 bar, which reduces maximum temperature differences by 16.7%.

Thermal stresses from differential expansion during cyclic operation and coefficient of thermal expansion (CTE) mismatches lead to cracking, material degradation, and disrupted electrochemical processes, resulting in voltage instability, reduced reliability, and limited commercial viability. To address these challenges, this study addresses the critical challenge of temperature non-uniformity in SOFCs by introducing three key advancements: (1) a novel six-channel active cooling system, uniquely designed to simultaneously reduce peak temperatures, enhance thermal uniformity, and stabilize voltage output; (2) the first systematic numerical evaluation of cooling parameters (flow rates, temperatures, co-/counter-current configurations) and their direct trade-offs on electrochemical performance (Nernst voltage, overpotentials); and (3) a practical framework to optimize cooling conditions for maximal voltage output and minimal thermal gradients. By bridging the gap between localized cooling strategies and system-level performance, this work provides actionable solutions to improve SOFC reliability and commercial viability, surpassing prior studies focused solely on passive geometric modifications.

2- Governing Equations and Modeling

This section outlines the fundamental equations governing the problem, including the conservation equations for mass, momentum, energy, electrochemical reactions, and chemical components. The assumptions considered are:

a) Fluid flow is laminar, steady, and incompressible, with pure hydrogen as fuel and air as the oxidizer flowing in the air channel.
b) Radiant heat transfer is neglected.
c) Local thermal equilibrium between fluid and solid is assumed.
d) The porous medium is considered uniform and isotropic.

2- 1- Conservation Equations

The equation of continuity for the steady flow is related to velocity field, **V** as follows [22]:

$$\nabla\cdot\left(\rho\mathbf{V}\right)=\sum_{i=a,c}S_i, \tag{1}$$

where ρ is the density of the mixture, which can be expressed as:

$$\rho=\left(\sum_{i=1}^{N}Y_i/\rho_i\right)^{-1} \tag{2}$$

Here, Y_i is the mass fraction of the i-th component, and ρ_i is the density of each component, which is calculated using the ideal gas law according to the partial pressure and molecular mass of that component.

The process begins with oxygen reduction at the cathode, producing oxygen ions (O^{2-}), which then react with hydrogen ions (H^{+}) to form water. The source terms S_i, for these reactions can be expressed as follows [22-24]:

$$S_a=S_{H_2}+S_{H_2O} \tag{3}$$

$$S_{H_2}=-\frac{i_{a,v}}{2F}M_{H_2} \tag{4}$$

$$S_{H_2O}=+\frac{i_{a,v}}{2F}M_{H_2O} \tag{5}$$

$$S_c = S_{O_2} \tag{6}$$

$$S_{O_2} = -\frac{i_{c,v}}{4F} M_{O_2} \tag{7}$$

where $i_{a,v}$ and $i_{c,v}$ are equal to the volumetric current density of anode and cathode, respectively. F is Faraday's constant and M_{H_2}, M_{O_2} and M_{H_2O} are equal to the molecular mass of hydrogen, oxygen and water, respectively. In a SOFC, the continuity equation represents the conservation of mass for species participating in the electrochemical reactions at the anode and cathode. The species conservation equations for the anode and cathode electrodes are formulated based on Fick's law, which describes mass transport and component conservation. These equations can be written as [22-24]:

$$\nabla.\left(\rho \mathbf{V} Y_i\right) = -\nabla.j_i + S_i \tag{8}$$

In Eq. (8), j_i is the multicomponent diffusion flux, which is calculated according to Fick's law [25, 26]:

$$j_i = -\sum_{j=1}^{N-1} \rho D_{ij} \nabla Y_j \tag{9}$$

which is defined in the porous medium as follows:

$$j_i = -\sum_{j=1}^{N-1} \rho D_{DG}^{eff} \nabla Y_j \tag{10}$$

where N is the total number of gas components, D_{ij} is the multicomponent diffusion coefficient and D_{DG}^{eff} is the dusty gas diffusion coefficient [27]. In flow regimes where viscous forces hold sway over convective forces, the momentum equation for porous media can be transformed from the Navier-Stokes equation to the Brinkman equation. This transformation is achieved by omitting the convective term and incorporating a new term that accounts for pressure drops in porous media, as described by Darcy's law. By incorporating this term into the Navier-Stokes equation, we arrive at the Brinkman equation [22]:

$$\mathbf{V} \cdot \nabla\left(\frac{\mathbf{V}}{\varepsilon^2}\right) = -\frac{\nabla P}{\rho} - \frac{\upsilon}{K}\mathbf{V} + \upsilon_{eff} \nabla^2\left(\frac{\mathbf{V}}{\varepsilon}\right) + \mathbf{G} \tag{11}$$

where P is the pressure, υ is the fluid's kinematic viscosity (subscript of *eff* stands for the effective value), ε is the porosity K is the permeability of the porous medium and **G** represents the body forces.

The omission of radiation effects in thermal simulations of SOFCs with lengths below 2 cm is justified by several factors. At smaller dimensions and moderate temperatures, heat transfer is dominated by conduction and convection rather than radiation, as the short optical path length in compact designs significantly reduces radiative heat exchange between surfaces. Additionally, the low surface emissivities of dense ceramic components, such as Yttria-Stabilized Zirconia (YSZ) electrolytes, further suppress radiative transfer. Hence, for shorter fuel cells, the contribution of radiation is minimal compared to other modes of heat transfer, enabling simplified simulations with sufficient accuracy. [28-30]. The energy equation for electrodes is formulated assuming local thermal equilibrium between the gas phase and porous medium [31]:

$$\nabla \cdot \left(\left(\rho c_p^{eff}\right)\mathbf{V}T\right) = \nabla.\left(k^{eff} \nabla T\right) + S_T \tag{12}$$

where c_p^{eff} is the effective specific heat of the gas at constant pressure, k^{eff} is the effective thermal conductivity for the porous medium.

$$\left(\rho c\right)_p^{eff} = \varepsilon\left(\rho c\right)_{p,f} + \left(1-\varepsilon\right)\left(\rho c\right)_{p,s} \tag{13}$$

$$k^{eff} = \varepsilon k_f + \left(1-\varepsilon\right)k_s \tag{14}$$

where the subscripts f and s are for fluid and solid, respectively. Also, S_T in the last term on right hans side of Eq. $\nabla \cdot \left(\left(\rho c_p^{eff}\right)\mathbf{V}T\right) = \nabla.\left(k^{eff} \nabla T\right) + S_T$ (12) is the heat source caused by the electrochemical reaction, ohmic, activation and concentration overpotentials [31].

In a fuel cell, electric and ionic charge transfer occurs simultaneously. In interconnections, only electric charge transfer and in electrolyte only ionic charge transfer occur. The charge transfer equations in the anode and cathode electrodes are as follows [32]:

$$\nabla.\left(\sigma_i \nabla \phi_{el}\right) = -i_{i,v}, \quad i = a, c \tag{15}$$

where σ_a and σ_c represent the electrical conductivities of the anode and cathode, respectively[33], and ϕ_{e_l} is the electrical exchange potential. Also, ionic charge transfer in electrolyte is given by:

$$\nabla.\left(\xi_{mem} \nabla \phi_{io}\right) = 0 \tag{16}$$

where subscript *mem* refers to the electrolyte, ξ_{mem} represents the ionic conductivity of the electrolyte and ϕ_{io} denotes the ionic potential in the electrolyte phase. Likewise, the mechanism of ionic charge transfer in the electrodes is

governed by:

$$\nabla.\left(\xi_i \nabla \phi_{io}\right) = i_{i,v}, \quad i = a,c \tag{17}$$

where ξ_a, ξ_b are respectively the ionic conductivities of the anode and cathode, respectively.

2- 2- Voltage and Overpotentials

In a SOFC, the local Nernst potential V_n is calculated at each electrode surface point using the local partial pressures of reacting species. This voltage depends on the Gibbs free energy, operating temperature, and reactant partial pressures, defining the maximum theoretical voltage [34].nFor hydrogen oxidation at the anode, the Nernst potential is expressed as:

$$V_n = -\frac{\Delta G^0_{f,h_2o}}{2F} + \frac{RT}{2F} ln\left(\frac{P_{H_2} P_{O_2}{}^{0.5}}{P_{H_2O}}\right) \tag{18}$$

$$\Delta G^0_{f,H_2O} = -247.4 + 0.0541T \tag{19}$$

where $\Delta G^0_{f,H_2O}$ is the Gibbs free energy for the reaction of water formation, and P_{H_2}, P_{O_2} and P_{H_2O} are the partial pressures of hydrogen, oxygen, and water, respectively. The average Nernst voltage $\overline{V}_n$, can then be obtained by area-averaging the local values over the electrode surface.

When a fuel cell operates in an electric circuit, it experiences voltage losses due to activation, ohmic, concentration, fuel, and electron transport limitations, causing deviation from ideal performance.

2- 2- 1- Activation Overpotential

The activation overpotentials at the anode and cathode electrodes, $\eta_{act,a}$ and $\eta_{act,c}$ can be calculated using the Butler–Volmer equation [22]. This equation relates the local overpotential to the interfacial current density at the electrode-electrolyte interface, allowing for accurate computation of activation losses:

$$i_a = i_{0,a}\left[exp\left(\frac{\alpha^a_a F \eta_{act_a}}{RT}\right) - exp\left(-\frac{\alpha^a_c F \eta_{act_a}}{RT}\right)\right] \tag{20}$$

$$i_c = i_{0,c}\left[exp\left(\frac{\alpha^c_a F \eta_{act_c}}{RT}\right) - exp\left(-\frac{\alpha^c_c F \eta_{act_c}}{RT}\right)\right] \tag{21}$$

where $i_{0,a}$ and $i_{0,c}$ are the exchange current density in the anode and cathode, respectively. α^a_a and α^a_c are the anodic and cathodic charge transfer coefficients in the anode electrode, and α^c_a and α^c_c are the anodic and cathodic charge transfer coefficients in the cathode electrode, which are usually considered 0.5 or given by equations [35]. The equation for estimating the exchange current density includes exponential coefficients for the anode ψ_a, and cathode ψ_c, reference pressure P^{ref}, and activation energy values for both electrodes, $E_{act,a}$ *and* $E_{act,c}$ [36]:

$$i_{0,a} = \psi_a \left(\frac{P_{H_2}}{P^{ref}}\right)\left(\frac{P_{H_2O}}{P^{ref}}\right)^{0.5} exp\left(\frac{-E_{act,a}}{RT}\right) \tag{22}$$

$$i_{0,c} = \psi_c \left(\frac{P_{O_2}}{P^{ref}}\right)^{0.25} exp\left(\frac{-E_{act,c}}{RT}\right) \tag{23}$$

In this context, i_a and i_c represent the local interfacial current density normal to the electrode surface. To compute the total activation loss, the local activation overpotential $\eta_{act(r)}$ is first calculated at each point along the electrode-electrolyte interface using the Butler–Volmer equation. The average activation loss $\overline{\eta}_{act_{a,c}}$ is then determined by integrating or averaging the local values across the entire electrode surface.

2- 2- 2- Ohmic Overpotential

The occurrence of ohmic overpotential stems from the internal resistance of the electrolyte against ion passage and resistance within the electrodes and connections to electric current flow. The local ohmic overpotentials throughout the domain are computed as: [37]:

$$\eta_{ohm}(\mathbf{r}) = \frac{\mathbf{i}(\mathbf{r})}{\sigma_{eff}} \cdot d\mathbf{l} \tag{24}$$

where σ_{eff} denotes the effective conductivity (electronic in electrodes and ionic in the electrolyte, and $d\mathbf{l}$ is a differential vector element that represents an infinitesimally small segment of a path along electric field. The total ohmic voltage drop across the cell is obtained by integrating the electric field along the dominant current path through the electrolyte, $\overline{\eta}_{ohm}$.

2- 2- 3- Concentration Overpotential

In a SOFC, the local concentrations and partial pressures of fuel and oxygen vary along the electrode surface due to consumption in electrochemical reactions, as well as aeration rate, fueling rate, and channel geometry. These spatial variations lead to local concentration overpotentials , which are evaluated based on the deviation of reactant concentrations at the electrode interface from their bulk values. The magnitude of the local concentration overpotential depends on factors such as reactant flow rate, electrode microstructure, material properties, and the design of flow channels [38].

Table 1. Input parameters related to the electrochemical reactions, electrolyte, and tortuosity [39-42].

Anode exchange current density A/m^2	5500
Cathode exchange current density A/m^2	5500
H_2 reference value	1
O_2 reference value	1
H_2O reference value	1
Anode tortuosity	3
Cathode tortuosity	3

Table 2. Electrical parameters including anode and cathode conductivity and interfaces contact resistance [22].

Anode electrical conductivity 1/Ω.m	30384
Cathode electrical conductivity 1/Ω.m	12872
Electrical conductivity of interconnections 1/Ω.m	3078
The resistance of the anode-interconnection interface Ω.m^2	1×10^{-7}
The resistance of the cathode-interconnection interface Ω.m^2	1×10^{-8}

$$\eta_{conc,a} = -\frac{RT}{2F} ln\left(\frac{P_{H_2O}P^{ref}_{H_2}}{P^{ref}_{H_2O}P_{H_2}}\right) \quad (25)$$

$$\eta_{conc,c} = \frac{RT}{4F} ln\left(\frac{P^{ref}_{O_2}}{P_{O_2}}\right) \quad (26)$$

Once these local values are obtained, they can be integrated or area-averaged over the electrode surface to determine the average concentration loss, $\bar{\eta}_{conc,a,c}$.

Based on the overpotential contributions described above, the overall output voltage of the fuel cell is calculated as:

$$\bar{V} = \bar{V}_n - \left(\bar{\eta}_{act,a} + \bar{\eta}_{act,c} + \bar{\eta}_{ohm} + \bar{\eta}_{conc,a} + \bar{\eta}_{conc,c}\right) \quad (27)$$

3- Model Settings

In the SOFC modeling setup, the Unresolved Electrolyte model and species transfer option are used. Electrochemical reactions are calculated using the volume option, with parameters including electrolyte thickness, zero fuel passage overpotential, current range (0–0.8 A), and electrolyte resistance (0.1948 Ω/m). Reaction headings and tortuosity follow Table 1, while contact resistance, voltage, and current settings are based on Table 2. Anode and cathode viscous resistances are set to 1×10^{-8} m^{-2}.

3- 1- Thermophysical and Electrical Properties of Fuel Cell Materials

In the materials section, a gas mixture of H_2O, O_2, H_2 and N_2 is defined, with properties including density, specific heat, thermal conductivity, mass diffusion, thermal diffusion, and electrical diffusion detailed using various laws and a user-defined function (UDF). Solid materials for the anode, cathode, electrolyte, and interconnections are specified from [22].

3- 2- Boundary Conditions

Boundary conditions aligned with practical fuel cell conditions are outlined in Table 3. Symmetry conditions depicted in Fig. 1 are employed to expedite calculations. Boundary conditions for electric potential in UDS0 dictate that the voltage and current tap surfaces match the current value and zero, respectively. The conditions of hydrogen and air input are also considered according to Table 4.

3- 3- Solution Method

A SIMPLE algorithm couples pressure and velocity fields, and the Rhie-Chow distance base scheme is used to calculate fluxes. The discretization of momentum, species transfer, energy, and electric potential equations is carried out with a first-order upwind scheme. The SIMPLE algorithm is chosen because it efficiently handles pressure-velocity coupling, which is critical in SOFC simulations where flow velocities are relatively low, ensuring stable and mass-conservative solutions. First-order discretization is selected

Table 3. Boundary conditions of the problem.

Boundary name	Boundary type	Description
Fuel inlet	Mass Flow Inlet	---
Air inlet	Mass Flow Inlet	---
Fuel outlet	Pressure Outlet	---
Air outlet	Pressure Outlet	---
Voltage Tap Surface	Wall	Anode connection terminal in connection with the circuit
Current Tap Surface	Wall	Cathode connection terminal in connection with the circuit
Electrolyte	Wall	Common plate between anode and cathode
Wall-CC-Anode	Wall	Connection between the anode and the interconnection to pass the electron
Wall-CC-Cathode	Wall	Connection between the cathode and the interconnection to pass the electron
Anode-Symmetry	Symmetry	Anode sidewalls for symmetry
Cathode-Symmetry	Symmetry	Cathode sidewalls for symmetry
Interconnection-Symmetry	Symmetry	Four interconnection sidewalls for symmetry
Channel-Symmetry	Symmetry	Two outer and side walls of the channels for symmetry

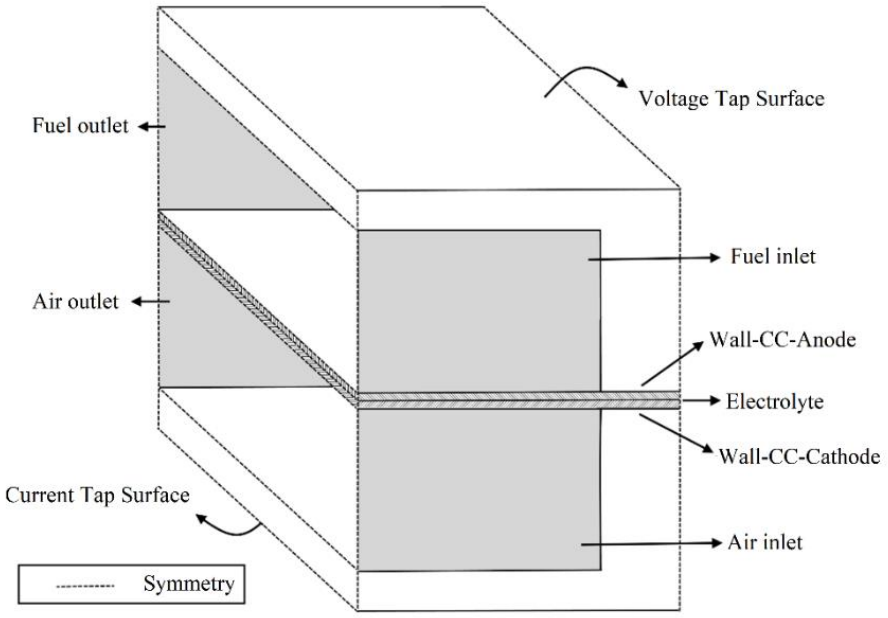

Fig. 1. Boundary conditions applied in the fuel cell.

Table 4. Air and fuel inlet conditions.

	Inlet mass flow rate (kg/s)	Inlet temperature (K)	Inlet mass fraction
Fuel	2.03×10^{-8}	1173	0.5 H_2 and 0.5 H_2O
Air	2.38×10^{-6}	1173	0.233 O_2

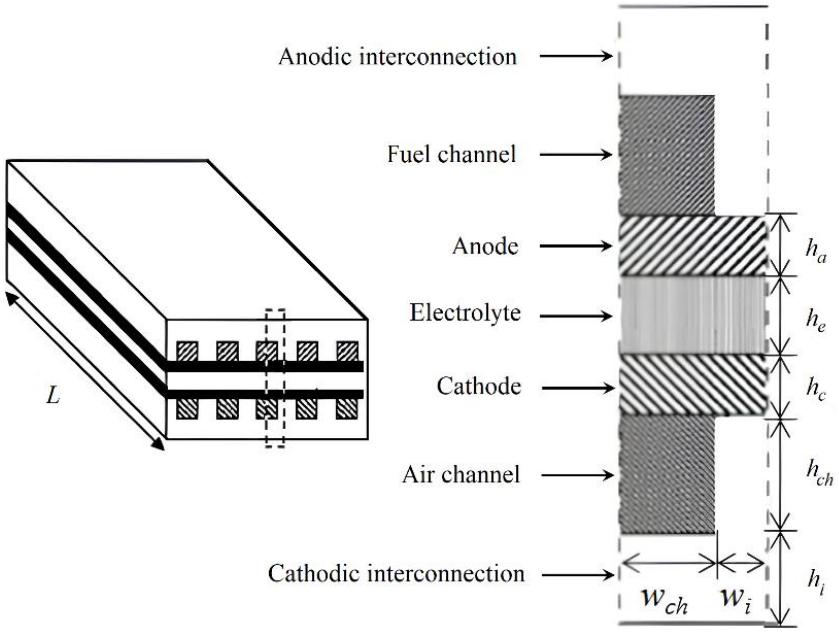

Fig. 2. Schematic of SOFC in the base case [43].

for its robustness and computational efficiency, particularly during the initial stages of simulation when source terms are not yet applied, allowing for faster convergence of the initial velocity and temperature fields. Initially, problem-solving occurs without source terms to converge the initial velocity and temperature fields, followed by the incorporation of source terms related to species transfer upon convergence. Electric and energy sources are introduced, and calculations are performed at zero current. Subsequently, current is incrementally increased until reaching the final value with the convergence of the problem.

4- Results and Ddiscussion

This section delves into analyzing the performance of a planar SOFC to determine Nernst voltage, output voltage, assess the maximum temperature difference within the PEN structure ΔT_{max}, and evaluate temperature gradients (the temperature gradient means its vector size at any point). Initially, the base case is established and numerical results are validated before examining the effects of cooling channel on the thermo-electrical performance of the fuel cell.

4- 1- Problem Definition

Fig. 2 depicts a planar fuel cell configuration, featuring anode and cathode interconnections, anode, cathode, and fuel and air channels, while excluding the electrolyte's physical presence. The study employs Ansys Design Modeler for geometry creation, Ansys Meshing for mesh generation, and Ansys Fluent for computational analysis.

ANSYS Fluent is particularly suited for simulating the thermal behavior of SOFCs due to its capability to handle complex, three-dimensional, laminar flow simulations and accurately model heat transfer mechanisms such as conduction and convection. Its robust multi-physics modeling capabilities, enhanced by customizable UDFs for material properties and boundary conditions, enable precise analysis of SOFC processes. The geometric dimensions, adopted from Christman et al.[43], are listed in Table 5 and serve as the baseline for the simulations.

4- 2- Mesh Independency and Model Validation

Mesh independence was validated through systematic grid refinement studies using five meshes with 5,670, 17,280, 50,400, 100,800, and 201,600 cells, monitoring fuel cell output voltage as the key metric. The results showed maximum voltage differences of 3.6% (9 mV) between the coarsest (5,760 cells) and finest (201,600 cells) meshes at high current densities, while low current densities were minimally affected. Further validation using 52,000, 104,420, and 201,600 cells under temperature-dependent exchange current density and cooling channel conditions (inlet temperature 1000 K, mass flow rate 1×10^{-5} kg/s) demonstrated voltage differences decreasing from 1.65% (52,000 to 104,420 cells) to 0.6% (104,420 to 201,600 cells) at 20,000 A/m². Finally, the mesh structure with the specified number of nodes in different dimensions is selected according to Table 6. A sample of the produced mesh is shown in Fig. 3. Based on these results, the optimal mesh sizes were selected as 100,800 cells for the basic case (without cooling channel) and 104,420 cells for cases with cooling channels, ensuring both computational efficiency and solution accuracy (voltage variations <1% for the finest meshes) while meeting minimum grid resolution requirements.

Comparison with Christman et al. [43] showed excellent

Table 5. Geometric dimensions of the fuel cell.

Parameter	Size (mm)
Length of the fuel cell, L (in the x direction).	20
Anode thickness, h_a (in the y direction).	0.05
Cathode thickness, h_c	0.05
Electrolyte thickness, h_e	0.15
The thickness of interconnections, h_i	0.5
Channel thickness, h_{ch}	1
Channel width, w_{ch} (in the z direction).	1.5
The width of interconnections, w_i	0.25

Table 6. Number of nodes for the base case condition.

Section	**Number of nodes**
Fuel cell length (in the x direction).	100
Outer width of each interconnection (in the z direction).	24
The width of the channels	18
The common border of interconnections and electrodes (in the z direction).	6
The width of the electrodes	24
The large outer height of each interconnection (in the y direction).	15
Small outer height of each interconnection	3
Height of channels	12
Height of the electrodes	6

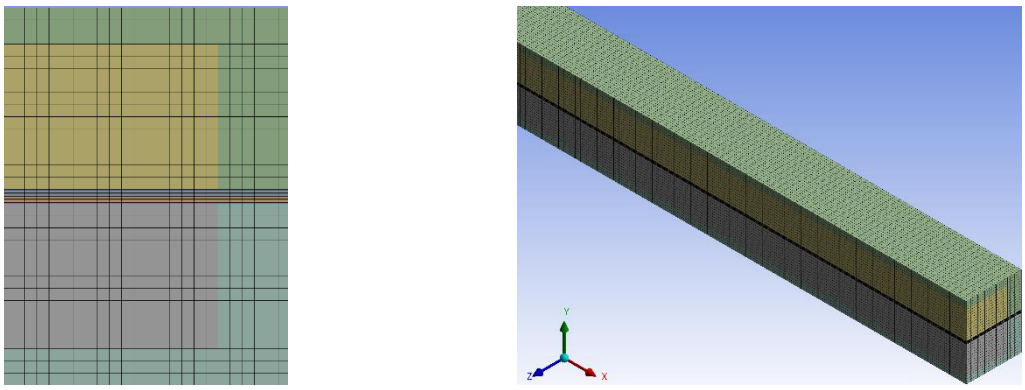

b a

Fig. 3. An illustration of the generated mesh is shown in two views: a) a 3D representation and b) a 2D projection

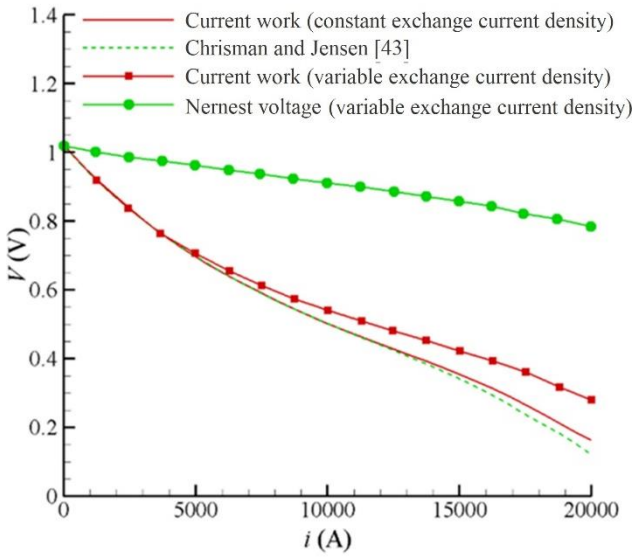

Fig. 4. Comparison of the output voltage between the present work and the results of Christman et al. [43].

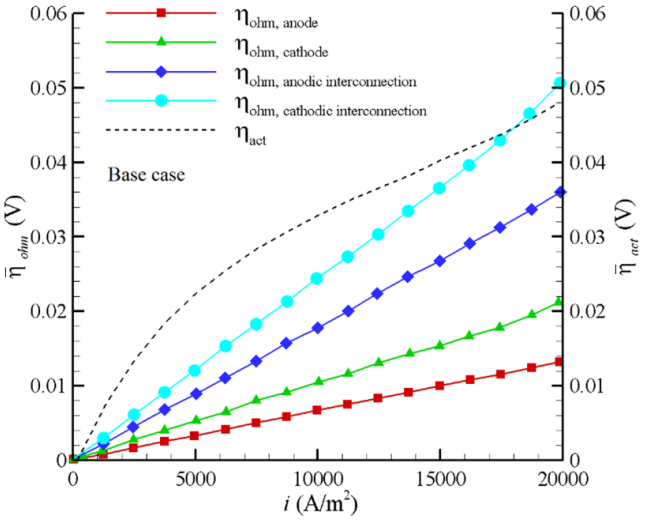

Fig. 5. Changes in the activation and ohmic overpotential changes in different parts of the fuel cell in the base case.

voltage agreement at low current densities, but significant deviations emerged above 15,000 A/m², reaching 27% difference at 20,000 A/m² (Fig. 4). This growing discrepancy stems primarily from differing approaches to over potential calculations. While Christman et al. assumed a temperature-independent exchange current density (i_0), our model incorporates temperature-dependent i_0, which becomes increasingly important at higher current densities where temperature rises substantially. This key difference leads to more accurate prediction of activation over potentials in our work. Furthermore, variations in modeling concentration over potentials (due to different transport approaches) and temperature-sensitive ohmic losses contribute to the observed deviation at high current densities.

4- 3- Base Case

Voltage analysis of the electrolyte plate for the base case (with temperature-dependent exchange current density) showed a decline in fuel cell output voltage from 1.0197 V to 0.2782 V as current density increased to 20,000 A/m², due to higher working temperatures, increased ohmic losses, and reduced species partial pressure (See Fig. 4). However, with a temperature-dependent exchange current density, the output voltage rose from 0.1634 V to 0.2782 V at i=20,000 A/m² as cell temperature increased. This is attributed to accelerated reaction rates at the electrodes, providing more active sites and increasing the exchange current density, i_0.

Rising temperature improves the electrolyte's conductivity and diffusion coefficient, enhancing ionic transport and charge transfer, which boosts output voltage while reducing activation over potential (the energy needed to activate electrodes). The voltage drop in the fuel cell is

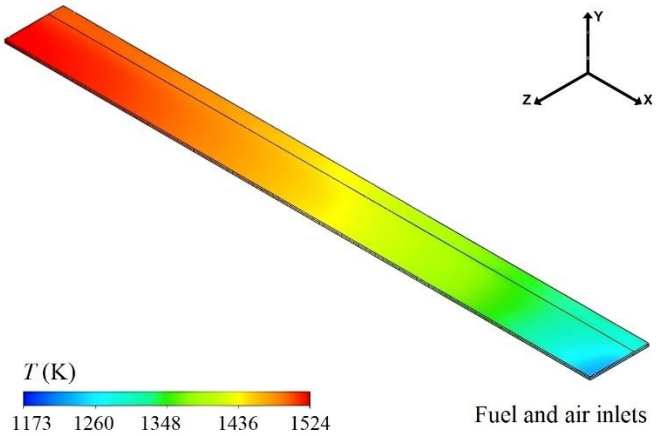

Fig. 6. Temperature distribution within the PEN structure in the base case.

primarily caused by over potentials, with activation over potential peaking at *~0.0467 V* at maximum current density (Fig. 5). Both anode and cathode exhibit similar activation over potential trends due to identical conditions. Ohmic over potential varies linearly with current density, with the highest loss in the cathode interconnection and the lowest in the anode (Fig. 5). Temperature distribution analysis of the PEN structure shows a gradient along air/fuel channels, influenced by ohmic losses and electrochemical reactions (Fig. 6). At 20,000 A/m², temperatures range from 1224.8 K (minimum) to 1523.7 K (maximum), yielding a 298.9 K difference (Fig. 7).

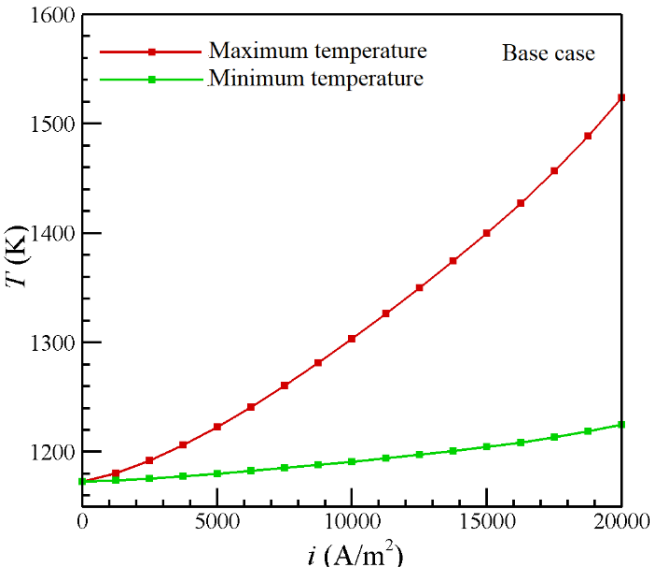

Fig. 7. Variation of maximum and minimum temperatures of the PEN in the base case.

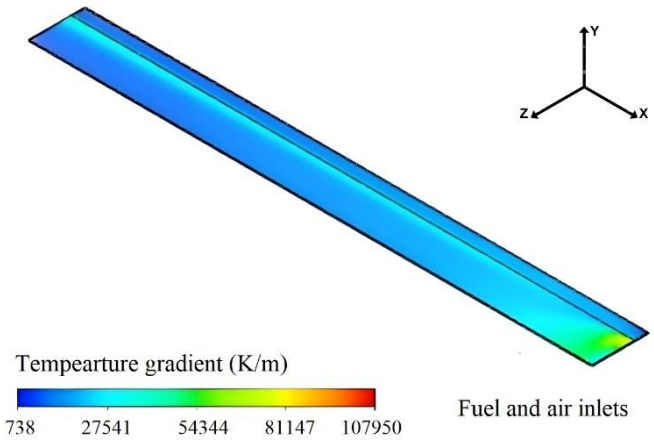

Fig. 8. Temperature gradient contour of the PEN in the base case.

The temperature gradient contour for the base case under a current density of 20,000 A/m² is displayed in Fig. 8, revealing a maximum temperature gradient of 107950 K/m. Notably, the highest gradient occurs near the fuel and air inlets and in proximity to interconnections and electrodes.

Examining only the maximum temperature difference and the maximum temperature gradient within the PEN is insufficient to assess temperature uniformity. A low temperature difference might still involve abrupt changes leading to a high gradient, or a low gradient might coexist with a substantial temperature difference. The Non-Uniformity Factor (*NUF*) is a quantitative measure used to assess the uniformity of temperature distribution within a system by integrating both the maximum temperature difference (ΔT_{max}) and maximum temperature gradient (∇T_{max}). Unlike evaluating ΔT_{max} or ∇T_{max} independently, the *NUF* provides a more comprehensive assessment, as a system could have a low ΔT_{max} but high ∇T_{max} (indicating localized hotspots) or vice versa. The *NUF* is necessary because it prevents misleading conclusions from single-parameter analyses, ensuring a more accurate evaluation of thermal performance. This study defines *NUF* to assess temperature distribution uniformity:

$$NUF = \left(\frac{\Delta T_{max}}{\Delta T_{max,b}}\right)\left(\frac{\nabla T_{max}}{\nabla T_{max,b}}\right) \tag{28}$$

where subscript *b* refers to the base case.

According to the *NUF* definition, a value of 1 represents the base case, with higher values indicating less uniform temperature distribution compared to the base case, and values lower than 1 signifying a more uniform temperature distribution relative to the base case. The *NUF* values will be presented in Table 7 to enable a comparison of various cooling modes in terms of temperature uniformity.

4- 4- Fuel Cells with Cooling Channel

To regulate the maximum temperature difference in the PEN structure, six cooling channels have been deployed in two sets of three channels within the anode and cathode interconnections, each measuring 2×1.5 mm². These cooling channels facilitate varying air flows with different temperatures and velocities in a co-current arrangement with the flow of air and fuel (see Fig. 9).

4- 4- 1- Effect of Cooling Air Temperature

The cooling channels operate with air flows at cooling temperatures of $T_{cooling}$=600, 800, and 1000 K, maintaining ideal gas parameters for density and using a power law for viscosity of the air fluid. The mass flow rate of cooling air varies at $\dot{m}_{cooling} = 1\times10^{-5}$, 1×10^{-6} and 1×10^{-7} kg/s. In Fig. 10, Nernst voltage variations are depicted concerning current density for the fuel cell under the base case condition and with cooling channels at a mass flow rate of 1×10^{-6} kg/s and cooling temperatures of 600, 800, and 1000 K. Specifically, at zero current density in the base case, the Nernst voltage is 1.0197V, while the cooling channels yield values of 1.0489 V, 1.0387 V, and 1.0258 V, respectively. The increase in Nernst voltage with decreasing temperature can be justified according to Eq. (18). Because the Nernst voltage has an inverse relationship with temperature.

Fig. 11 shows that higher cooling temperatures improve the fuel cell's voltage output, but this effect changes with current. At low currents, heat helps most by speeding up

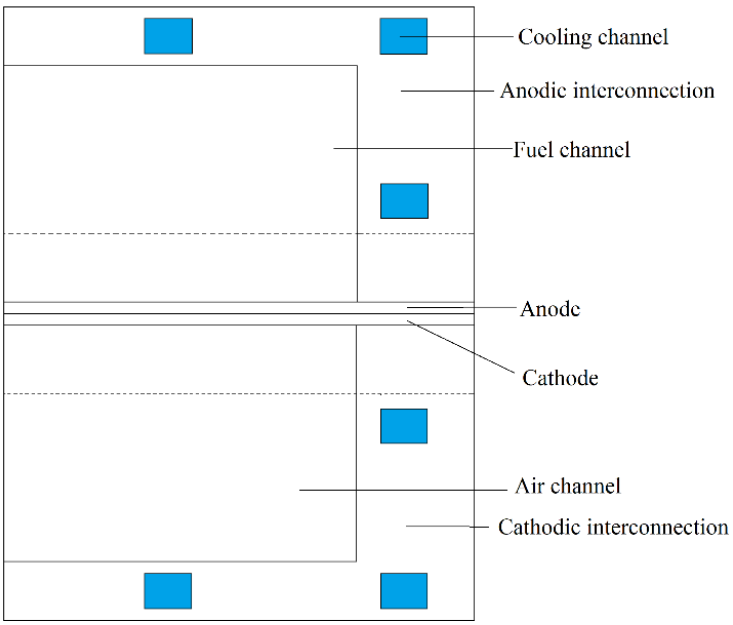

Fig. 9. Location of three cooling channels in the anodic interconnection and three cooling channels in the cathodic interconnection.

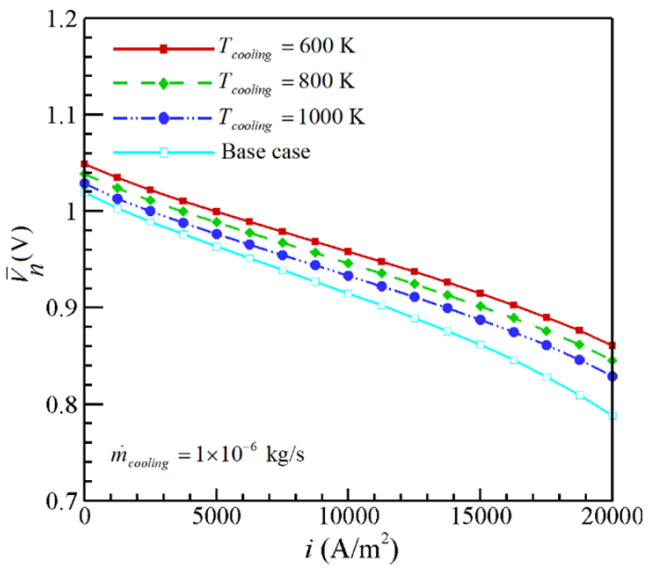

Fig. 10. Nernst voltage changes in base case and fuel cell with different cooling temperatures and mass flow rate of 1×10^{-6} kg/s

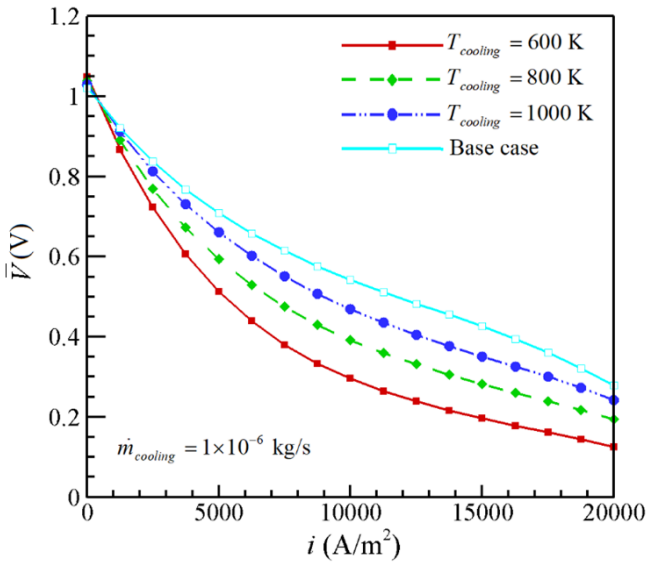

Fig. 11. Variations of output voltage at different cooling temperatures and the base case

the chemical reactions (reducing activation loss), so voltage increases sharply with temperature. At medium currents, heat still helps by making ions move easier, but resistance starts limiting further gains. At high currents, resistance dominates, so extra heat barely improves voltage. This explains why the lines in Fig. 11 spread apart at low currents but come closer together at high currents—temperature matters less when resistance takes over.

The activation overpotential is inversely affected by the exchange current density and worsens at lower temperatures. At 600 K, it reaches 0.1004 V, an 86.62% increase compared to the base case value of 0.0538 V (Fig. 12). As temperature decreases, ohmic overpotential rises due to the direct relationship between electrical conductivity and temperature

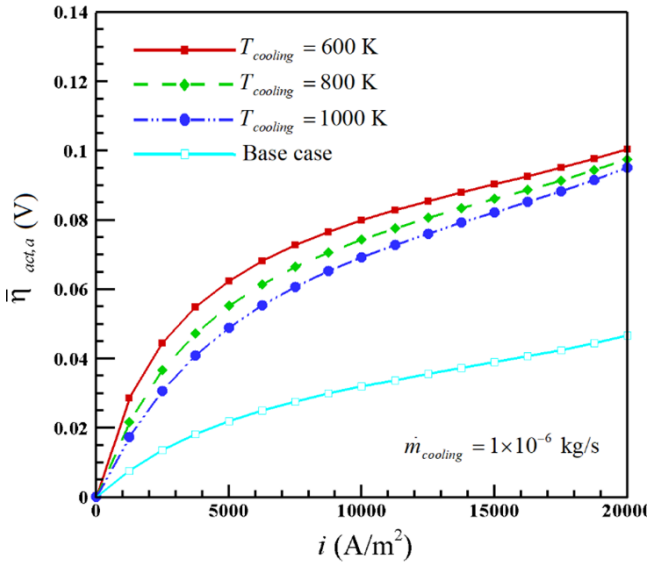

Fig. 12. Activation overpotential changes at different cooling temperatures and the base case.

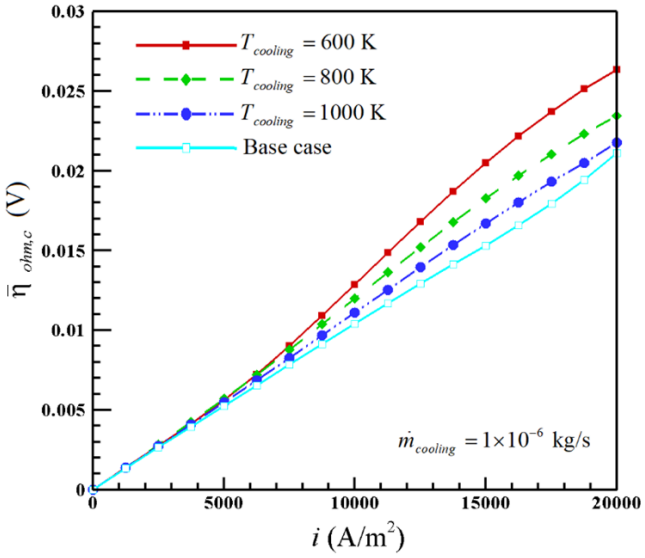

Fig. 14. Variations of ohmic overpotential in the cathode electrode with different cooling temperature and the base case.

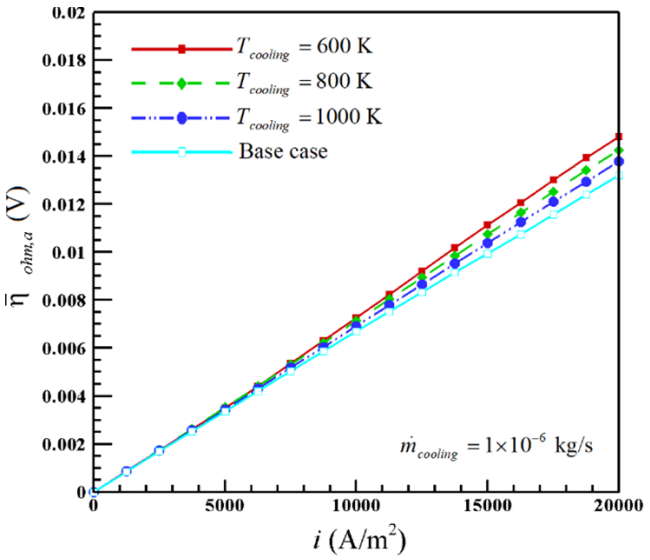

Fig. 13. Variations of ohmic overpotential in the anode with different cooling temperature and the base case.

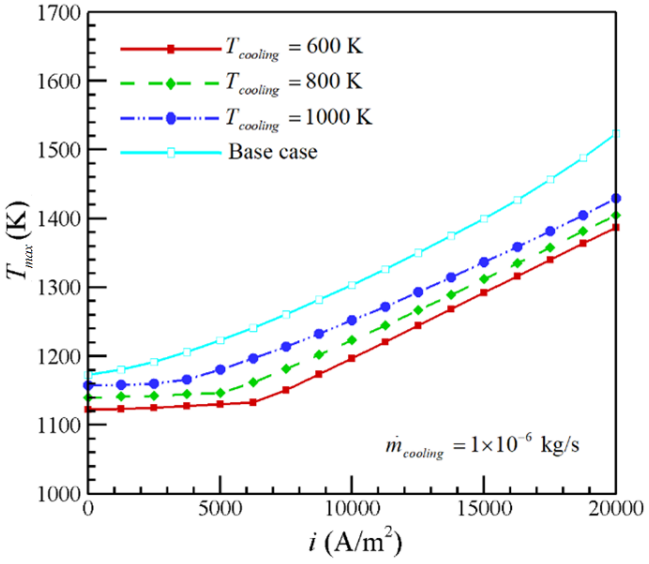

Fig. 15. Maximum temperature changes of the PEN in the base case and the presence of cooling flow with different temperatures and mass flow rate of 1×10⁻⁶ kg/s.

in the electrodes [38].

Variations in ohmic overpotential for the anode and cathode electrodes are shown in Fig. 13 and Fig. 14 for the base case and a fuel cell with cooling channels at inlet temperatures of 600, 800, and 1000 K.

These figures show increased ohmic losses in both electrodes compared to the base case. At 600 K cooling flow and a mass flow rate of 1×10⁻⁶ kg/s, the maximum PEN temperature drops to 1387.07 K, which is 136.66 K lower than the base case (Fig. 15). At lower current densities, the PEN's maximum temperature rises gradually; for example, with a 600 K inlet temperature, the increase is less than 10.23 K before reaching 6250 A/m². This trend is consistent for 800 K and 1000 K cooling, though the slope of temperature change increases at lower current densities with higher coolant temperatures. At higher current densities, the slope

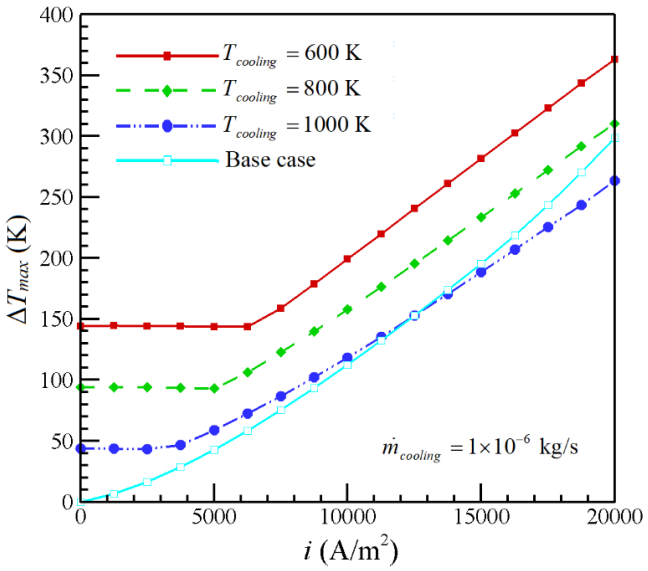

Fig. 16. Changes in the maximum temperature difference of PEN in the base case and the presence of cooling flow with different temperatures and mass flow rate of 1×10^{-6} kg/s.

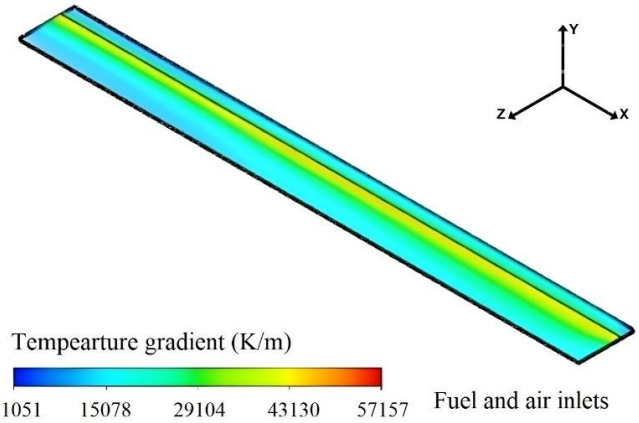

Fig. 17. Changes in the maximum temperature difference of PEN in the base case and the presence of cooling flow with different temperatures and mass flow rate of 1×10^{-6} kg/s.

closely matches the base case, indicating reduced cooling flow efficiency as current density rises.

The differences in maximum temperature trends between cooling and base case scenarios (Fig. 16) arise from active thermal management in cooling scenarios versus passive conditions in the base case. Higher cooling temperatures, such as 1000 K compared to 600 K, enhance heat removal efficiency by improving thermal conductivity and stabilizing heat distribution, thereby reducing thermal gradients and lowering the maximum temperature difference ΔT_{max}, across the fuel cell. In contrast, the base case lacks active cooling, resulting in uneven heat accumulation and a larger ΔT_{max} as current density increases. For instance, at 20,000 A/m², cooling at 1000 K reduces ΔT_{max} by 35.17 K compared to the base case. While lower cooling temperatures significantly reduce the PEN's maximum and minimum temperatures, they produce steeper gradients at low current densities than the base case. However, at medium to high current densities, ΔT_{max} under cooling increases linearly with current density, whereas the base case exhibits a non-linear rise with an escalating slope. The cooling system's ability to mitigate hotspots explains its flatter and more controlled ΔT_{max} trends compared to the steeper, less stable trends of the base case.

In a SOFC, temperature gradients represent the rate of temperature change across components. While some temperature variation is normal, high gradients prove problematic as they induce mechanical stresses from thermal expansion mismatches - potentially causing cracks or delamination in brittle ceramics - while also creating non-uniform reaction rates that reduce efficiency and accelerate degradation through electrode deactivation or seal failure. These effects are clearly demonstrated in Fig. 17, which shows temperature gradient distribution during cooling at 1000 K with a mass flow rate of 1×10^{-6} kg/s and current density of 20,000 A/m², where the maximum gradient reaches 57,156.5 K/m (57.2 K/mm) in the cathode and its interface with the interconnection.

4- 4- 2- Effect of Cooling Flow Rate

Cooling air can enter the channels at three mass flow rates—1×10^{-5}, 1×10^{-6}, and 1×10^{-7} kg/s—corresponding to Reynolds numbers of 172.9, 17.29, and 1.73, respectively. The impact of varying mass flow rates on the fuel cell's performance is examined at a cooling temperature of 1000 K. Increasing the mass flow rate decreases the fuel cell temperature, which raises the Nernst voltage but also increases overpotential or losses, as shown in Fig. 18. Excessively high cooling flow rates, exceeding ~5×10^{-5} kg/s for typical planar SOFCs, cause output voltage to collapse to near-zero by overcooling the cell below its operational temperature window. This impedes electrochemical processes, reduces ionic conductivity in the electrolyte (increasing ohmic losses), slows electrode reaction kinetics (raising activation overpotential), and induces mechanical stresses from thermal gradients that can crack components or delaminate interfaces.

For a mass flow rate of 1×10^{-5} kg/s and a current density of 13,750 A/m², the fuel cell's output voltage drops to zero. Reducing the mass flow rate increases temperature, reducing overpotentials; at 1×10^{-7} kg/s, the output voltage is 0.2676 V, which is 3.97% (0.0106 V) higher than the base case. At 1×10^{-5} kg/s and 13,750 A/m², activation overpotential is 0.0489 V higher than the base case, with ohmic overpotential differences of 0.0017 V (anode) and 0.004 V (cathode). The maximum PEN temperature difference remains around 105 K for 1×10^{-5} kg/s (Fig. 19). For 1×10^{-6} kg/s, the maximum temperature difference decreases by 35.17 K compared to

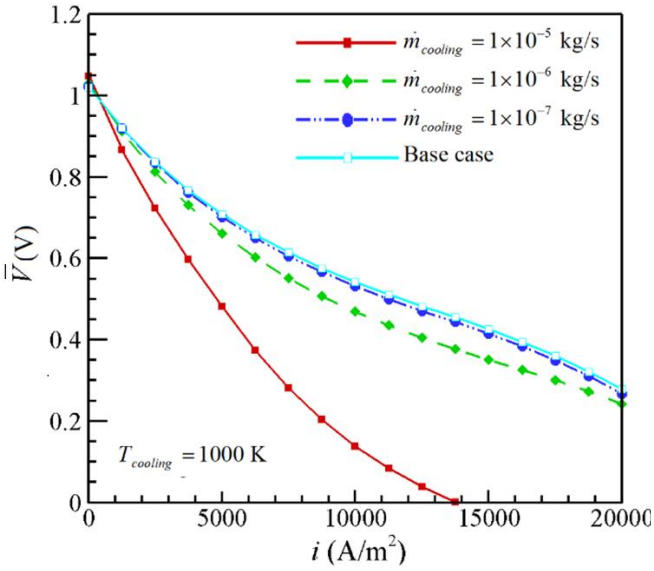

Fig. 18. Output voltage variation in the base case with cooling channels and different mass flow rates ($T_{cooling}$= 1000 K).

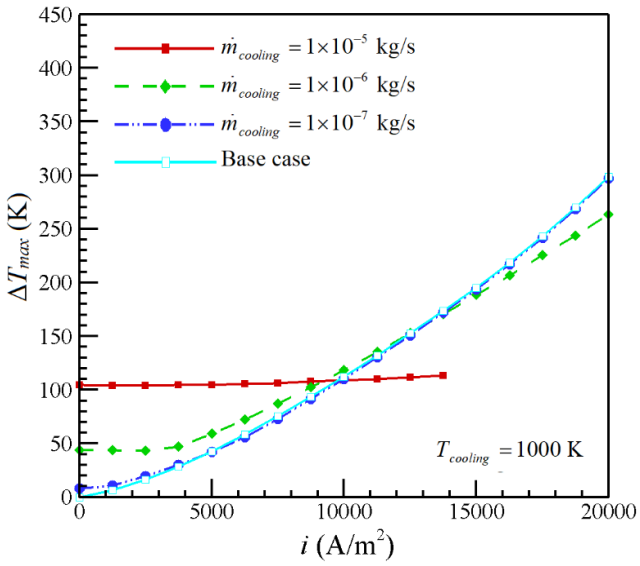

Fig. 19. Changes of ΔT_{max} in the base case and with cooling channels and different mass flow rates ($T_{cooling}$= 1000 K).

the base case, reaching 263.68 K at high current density. Lower mass flow rates and current densities below 10,000 A/m² further reduce PEN temperature differences. Changes in interconnections are minimal and omitted for brevity.

4- 4- 3- Effect of Cooling Flow Direction

In SOFCs, co-current cooling offers better cooling efficiency, lowering operating temperatures to reduce thermal stress but potentially decreasing ionic conductivity and output voltage at high current densities. In contrast, counter-current cooling provides more uniform temperature distribution, minimizing thermal gradients and improving reaction kinetics, which enhances performance at higher current densities despite less effective overall cooling. This section examines the impact of cooling flow direction (co-current and counter-current) at a mass flow rate of 1×10^{-6} kg/s and cooling temperatures of 600, 800, and 1000 K. For 1000 K cooling, the maximum output voltage in co-current mode is 1.0286 V, matching counter-current and base case values initially (Fig. 20). However, as current density increases, co-current mode shows the lowest output voltage due to superior cooling efficiency and lower temperatures. The base case outperforms counter-current cooling up to 17,841 A/m², beyond which counter-current mode provides higher voltages, peaking at 0.2933 V at maximum current density. This highlights tradeoffs between cooling efficiency and electrochemical performance.

Fig. 21 shows variations in the maximum temperature difference within the PEN structure for co-current and counter-current cooling at 1000 K and the base case. At low current density, the base case has the smallest temperature difference, but beyond 9,340 A/m² (counter-current) and

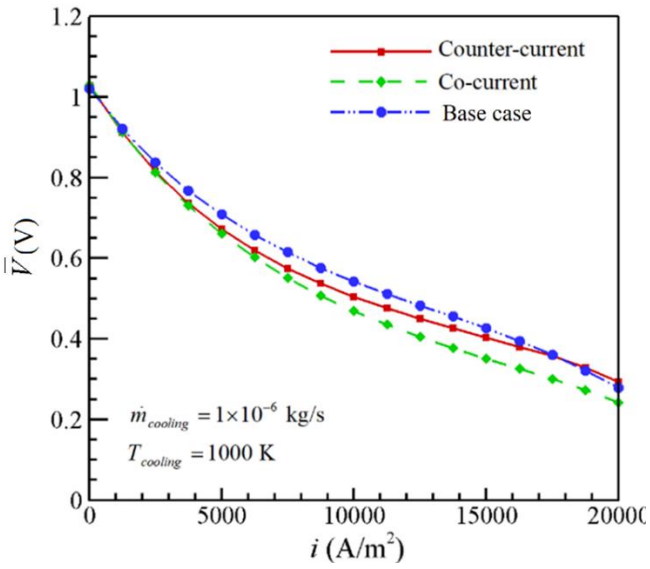

Fig. 20. Variations of the output voltage for co-current and counter-current cooling modes, at the cooling temperature of 1000 K and the base case.

12,483 A/m² (co-current), the PEN's maximum temperature difference drops below base case levels. Fig. 22 highlights that counter-current flow achieves more uniform PEN temperature distribution. At 800 K cooling, the Nernst voltage in counter-current mode is 1.0387 V, slightly lower than co-current mode. At maximum current density, the output voltage is 0.2802 V for counter-current cooling, higher than

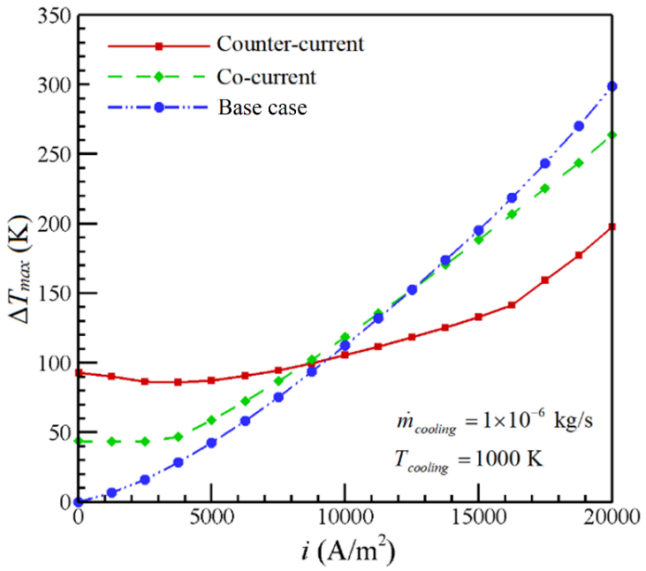

Fig. 21. Changes of the maximum temperature difference in the PEN for co-current and counter-current cooling flows, at the cooling temperature of 1000 K and the base case.

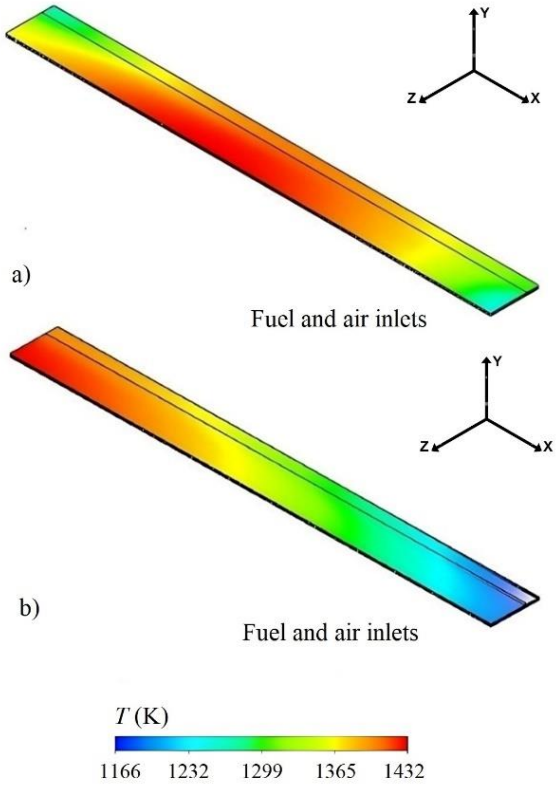

Fig. 22. Temperature contours in the PEN structure of the fuel cell for a) co-current and b) counter-current cooling flows at a cooling temperature of 1000 K and a current density of 20,000 A/m²

0.0867 V (co-current) and 0.0019 V (base case).

Fig. 23 illustrates the maximum temperature difference in the PEN, showing that the base case has a smaller temperature difference compared to co-current cooling. Counter-current cooling exhibits a large temperature difference at low current densities, but this diminishes beyond 13,856 A/m² when compared to co-current cooling. Similarly, beyond 16,928 A/m², the maximum temperature difference decreases relative to the base case.

Reducing the cooling fluid temperature to 600 K in counter-current cooling mode results in a Nernst voltage of 1.0488 V at zero current density, slightly lower than in co-current mode. At maximum current density, the output voltage is 0.2471 V, exceeding co-current mode by 0.1214 V but remaining 0.0311 V below the base case. The PEN's maximum and minimum temperatures in counter-current cooling are 1389.12 K and 1045.39 K, respectively, with a maximum temperature difference of 343.72 K (Fig. 24). The base case shows the smallest temperature difference, while counter-current cooling (below 18,236 A/m²) exhibits the highest. Comparing Fig. 21, Fig. 23, and Fig. 24 reveals that reducing cooling temperature significantly decreases the base case's temperature difference compared to other states, and counter-current cooling tends to reduce temperature differences at higher current densities.

The summary of numerical results related to the T_{max}, ΔT_{max}, ∇T_{max}, *NUF* and output voltage in 19 cases of simulation is given in Table 7. The important results obtained are listed in the conclusion section.

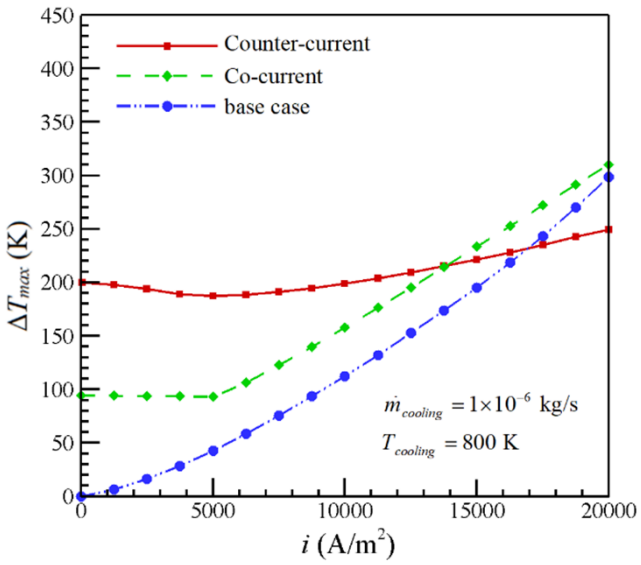

Fig. 23. Variation in the maximum temperature difference within the PEN structure under co-current and counter-current cooling at a coolant temperature of 800 K, relative to the base case

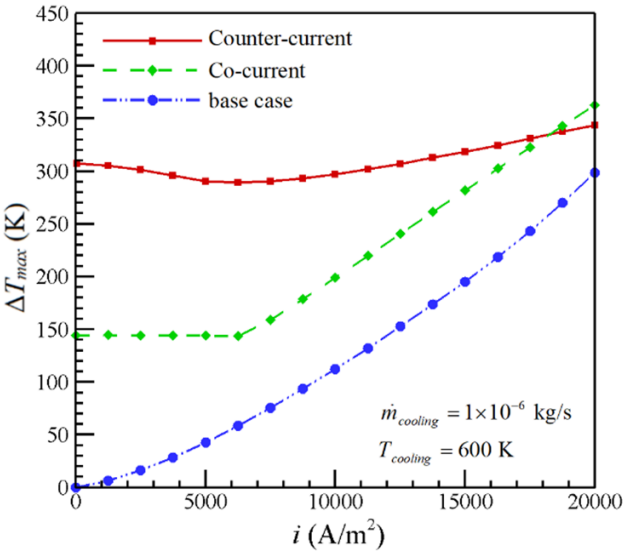

Fig. 24. Variation of the maximum temperature difference in the PEN structure under co-current and counter-current cooling at a cooling temperature of 600 K, compared to the base case.

5- Conclusion

This paper examined the thermo-electrical performance of a SOFC with six cooling channels, each measuring 2×1.5 mm², arranged in two sets in the anodic and cathodic interconnections. Cooling channels operated with air flows at temperatures of 600, 800, and 1000 K, and mass flow rates of 1×10^{-5}, 1×10^{-6}, and 1×10^{-7} kg/s, in co-current and counter-current configurations. Key findings and recommendations for future research include:

- The lowest maximum PEN temperature of 1387 K occurred in case 4 (co-current flow, $T_{cooling}$=600 K, mass flow rate=1×10^{-6} kg/s), while case 13 (counter-current, same conditions) reached 1389.11 K. These cases had the highest *NUF* values (2.33 and 1.96, respectively) and non-uniform temperature distributions of 133% and 96% compared to the base case.
- The minimum ΔT_{max} occurred in case 15 (counter-current flow, $T_{cooling}$ =1000 K, mass flow rate=1×10^{-6} kg/s), with the highest output voltage of 0.2933 V, surpassing the base case, and a 21.5% reduction in temperature non-uniformity.
- Increasing the cooling flow's mass flow rate and lowering electrode temperatures increased over potential losses,

Table 6. Summary of numerical results related to T_{max}, ΔT_{max}, ∇T_{max}, NUF and V in 19 simulation cases.

Flow arrangement	Case	Case number	$T_{cooling}$ (K)	T_{max} (K)	ΔT_{max} (K)	∇T_{max} (K/m)	*NUF*	$\bar{V}$ (V)
---	Base case	0	---	1523.73	298.9	107950	1	0.2782
Co-current	$\dot{m}=1\times10^{-7}$ kg/s	1	600	1509.14	293.2	44763.1	0.4067	0.2656
		2	800	1514.71	295.1	46612.7	0.4263	0.2668
		3	1000	1520.43	297.2	61295.5	0.5645	0.2676
	$\dot{m}=1\times10^{-6}$ kg/s	4	600	1387.07	362.7	207310	2.3303	0.1256
		5	800	1404.76	310.3	128876	1.2393	0.1934
		6	1000	1429.72	263.73	57156.5	0.4671	0.2421
	$\dot{m}=1\times10^{-5}$ kg/s	7	600	Output voltage vanishes at i=9800 A/m^2				
		8	800	Output voltage vanishes at i=10285 A/m^2				
		9	1000	Output voltage vanishes at i=13750 A/m^2				
Counter-current	$\dot{m}=1\times10^{-7}$ kg/s	10	600	1488.83	259.21	87013.7	0.6990	0.2758
		11	800	1498.67	268.64	87918	0.7319	0.2735
		12	1000	1510.89	280.46	88827	0.7720	0.271
	$\dot{m}=1\times10^{-6}$ kg/s	13	600	1389.11	343.7	184428	1.9645	0.2471
		14	800	1404.07	249.1	156979	1.2118	0.2802
		15	1000	1431.54	197.6	128100	0.7844	0.2933
	$\dot{m}=1\times10^{-5}$ kg/s	16	600	Output voltage vanishes at i=9860 A/m^2				
		17	800	Output voltage vanishes at i=10400 A/m^2				
		18	1000	Output voltage vanishes at i=13750 A/m^2				

causing output voltage to drop to zero before reaching maximum current density. In co-current arrangements, this occurred at current densities of 9800, 10285, and 13750 A/m² for cooling temperatures of 600, 800, and 1000 K, respectively, while counter-current arrangements showed a slight delay in this effect.

- Optimizing cooling channel designs and flow parameters through combined CFD simulations and experimental studies, while integrating machine learning for predictive modeling, could simultaneously refine channel geometry/flow rates for better thermal uniformity and enable real-time optimization of thermal-electrical performance with degradation prediction.
- Future investigations should explore alternative cooling fluids (Nano fluids, PCMs, or hybrid air-liquid systems) under dynamic operating conditions, including transient loads and variable fuel compositions (e.g., H_2-CH_4blends), to simultaneously improve heat dissipation and evaluate performance stability challenges.

Nomenclature

A_V	Active surface-to-volume ratio (m^{-1})
c_p	Specific heat (J/kg·K)
D	Multicomponent diffusion (m^2/s)
E_{act}	Activation energy values for anode and cathode (J/mol)
F	Faraday's constant (C/mol)
G	Gibbs free energy (J/mol)
$\boldsymbol{G}$	Body force (N·m/kg)
i	Current density (A/m^2)
i_0	Exchange current density (A/m^2)
j	Multicomponent diffusion flux ($kg/m^2 \cdot s$)
k	Thermal conductivity (W/m·K)
K	Permeability of the porous medium
$\mathbf{l}$	path along electric field (m)
M	Molecular mass (kg/kmol)
P	Pressure (Pa)
Q	Heat generation (W/m^2)
r	Area specific resistance ($\Omega \cdot m^2$)
R	Universal gas constant (J/mol·K)
S	Source term for electrochemical reactions ($kg/m^3 \cdot s$)
T	Temperature (K)
$\mathbf{V}$	Velocity field (m/s)
V	Local voltage (V)
$\overline{V}$	Average voltage (V)
Y	Mass fraction

Greek symbols

α	Anodic and cathodic charge transfer coefficients
δ	Thicknesses (m)
ε	Porosity of anode and cathode
η	Local overpotentials (V)
$\overline{\eta}$	Average overpotentials (V)
ξ	Ionic conductivity ($\Omega^{-1} \cdot m^{-1}$)
ν	Kinematic viscosity (m^2/s)
ρ	Density of the mixture (kg/m^3)
σ	Electrical conductivities ($\Omega^{-1} \cdot m^{-1}$)
ψ	Exponential coefficients for the anode and cathode

References

[1] L.-K. Chiang, H.-C. Liu, Y.-H. Shiu, C.-H. Lee, R.-Y.J.R.E. Lee, Thermo-electrochemical and thermal stress analysis for an anode-supported SOFC cell, 33(12) (2008) 2580-2588.

[2] H. Huo, K. Xu, L. Cui, H. Zhang, J. Xu, X. Kuang, Temperature gradient control of the solid oxide fuel cell under variable load, ACS omega, 6(42) (2021) 27610-27619.

[3] C. Schluckner, V. Subotić, S. Preißl, C. Hochenauer, Numerical analysis of flow configurations and electrical contact positions in SOFC single cells and their impact on local effects, International Journal of Hydrogen Energy, 44(3) (2019) 1877-1895.

[4] Z. Zeng, Y. Qian, Y. Zhang, C. Hao, D. Dan, W. Zhuge, A review of heat transfer and thermal management methods for temperature gradient reduction in solid oxide fuel cell (SOFC) stacks, Applied Energy, 280 (2020) 115899.

[5] Y. Ji, K. Yuan, J. Chung, Y.-C.J.J.o.P.S. Chen, Effects of transport scale on heat/mass transfer and performance optimization for solid oxide fuel cells, 161(1) (2006) 380-391.

[6] V.A. Danilov, M.O. Tade, A CFD-based model of a planar SOFC for anode flow field design, International Journal of Hydrogen Energy, 34(21) (2009) 8998-9006.

[7] R.M. Manglik, Y.N. Magar, Heat and mass transfer in planar anode-supported solid oxide fuel cells: effects of interconnect fuel/oxidant channel flow cross section, Journal of Thermal Science and Engineering Applications, 7(4) (2015) 041003.

[8] Q. Shen, L. Sun, B. Wang, Numerical simulation of the effects of obstacles in gas flow fields of a solid oxide fuel cell, International Journal of Electrochemical Science, 14(2) (2019) 1698-1712.

[9] R. Kumar, A. Veeresh Babu, S.H. Sonawane, Performance evaluation of a trapezoidal interconnector configuration of solid oxide fuel cell: A numerical study, International

Journal of Energy Research, 46(14) (2022) 19710-19722.

[10] J. Fan, J. Shi, R. Zhang, Y. Wang, Y. Shi, Numerical study of a 20-cell tubular segmented-in-series solid oxide fuel cell, Journal of Power Sources, 556 (2023) 232449.

[11] C. Gong, Z. Tu, S.H. Chan, A novel flow field design with flow re-distribution for advanced thermal management in Solid oxide fuel cell, Applied Energy, 331 (2023) 120364.

[12] W. Lee, M. Lang, R. Costa, I.-S. Lee, Y.-S. Lee, J. Hong, Enhancing uniformity and performance in Solid Oxide Fuel Cells with double symmetry interconnect design, Applied Energy, 381 (2025) 125178.

[13] Y. Inui, N. Ito, T. Nakajima, A.J.E.C. Urata, Management, Analytical investigation on cell temperature control method of planar solid oxide fuel cell, 47(15-16) (2006) 2319-2328.

[14] Y. Li, H. Yan, Z. Zhou, W.T.J.I.J.o.E.R. Wu, Three-dimensional nonisothermal modeling of solid oxide fuel cell coupling electrochemical kinetics and species transport, 43(13) (2019) 6907-6921.

[15] S. Sugihara, H. Iwai, Experimental investigation of temperature distribution of planar solid oxide fuel cell: effects of gas flow, power generation, and direct internal reforming, International Journal of Hydrogen Energy, 45(46) (2020) 25227-25239.

[16] E. Guk, V. Venkatesan, S. Babar, L. Jackson, J.-S. Kim, Parameters and their impacts on the temperature distribution and thermal gradient of solid oxide fuel cell, Applied Energy, 241 (2019) 164-173.

[17] J. Kupecki, K. Motylinski, A. Zurawska, M. Kosiorek, L. Ajdys, Numerical analysis of an SOFC stack under loss of oxidant related fault conditions using a dynamic non-adiabatic model, International Journal of Hydrogen Energy, 44(38) (2019) 21148-21161.

[18] D.H. Kim, Y. Bae, S. Lee, J.-W. Son, J.H. Shim, J. Hong, Thermal analysis of a 1-kW hydrogen-fueled solid oxide fuel cell stack by three-dimensional numerical simulation, Energy Conversion and Management, 222 (2020) 113213.

[19] Q. Xu, M. Guo, L. Xia, Z. Li, Q. He, D. Zhao, K. Zheng, M. Ni, Temperature gradient analyses of a tubular solid oxide fuel cell fueled by methanol, Transactions of Tianjin University, 29(1) (2023) 14-30.

[20] H. Jian, C. Hao, Z. Zeng, Y. Zhang, G. Wei, H. Jiang, Y. Qian, W. Zhuge, Y. Zhang, Reconstructing the distributions of temperature and temperature gradient of the solid oxide fuel cell based on several local temperatures, Applied Thermal Engineering, 272 (2025) 126458.

[21] C. Lin, F. Kerscher, S. Herrmann, B. Steinrücken, H. Spliethoff, Analysis on temperature uniformity in methane-rich internal reforming solid oxide fuel cells (SOFCs), International Journal of Hydrogen Energy, 57 (2024) 769-788.

[22] N. Akhtar, S.P. Decent, D. Loghin, K. Kendall, A three-dimensional numerical model of a single-chamber solid oxide fuel cell, International Journal of Hydrogen Energy, 34(20) (2009) 8645-8663.

[23] H. Zhu, R.J. Kee, Modeling electrochemical impedance spectra in SOFC button cells with internal methane reforming, Journal of The Electrochemical Society, 153(9) (2006) A1765.

[24] C.-Y. Wang, Fundamental models for fuel cell engineering, Chemical reviews, 104(10) (2004) 4727-4766.

[25] T. Berning, N. Djilali, Three-dimensional computational analysis of transport phenomena in a PEM fuel cell—a parametric study, Journal of Power Sources, 124(2) (2003) 440-452.

[26] B.R. Sivertsen, N. Djilali, CFD-based modelling of proton exchange membrane fuel cells, Journal of Power Sources, 141(1) (2005) 65-78.

[27] R. Taylor, R. Krishna, Multicomponent mass transfer, John Wiley & Sons, 1993.

[28] S.A. Hajimolana, M.A. Hussain, M. Soroush, W. Wan Daud, M. Chakrabarti, Modeling of a Tubular-SOFC: The Effect of the Thermal Radiation of Fuel Components and CO Participating in the Electrochemical Process, Fuel Cells, 12(5) (2012) 761-772.

[29] X. Xue, J. Tang, N. Sammes, Y. Du, Dynamic modeling of single tubular SOFC combining heat/mass transfer and electrochemical reaction effects, Journal of power sources, 142(1-2) (2005) 211-222.

[30] K. Daun, S. Beale, F. Liu, G.J.J.o.P.S. Smallwood, Radiation heat transfer in planar SOFC electrolytes, 157(1) (2006) 302-310.

[31] V.M. Janardhanan, O. Deutschmann, Numerical study of mass and heat transport in solid-oxide fuel cells running on humidified methane, Chemical Engineering Science, 62(18-20) (2007) 5473-5486.

[32] M. Saied, K. Ahmed, M. Ahmed, M. Nemat-Alla, M. El-Sebaie, Investigations of solid oxide fuel cells with functionally graded electrodes for high performance and safe thermal stress, international journal of hydrogen energy, 42(24) (2017) 15887-15902.

[33] Z. Zhang, J. Chen, D. Yue, G. Yang, S. Ye, C. He, W. Wang, J. Yuan, N. Huang, Three-dimensional CFD modeling of transport phenomena in a cross-flow anode-supported planar SOFC, Energies, 7(1) (2013) 80-98.

[34] M. Xu, T.S. Li, M. Yang, M. Andersson, I. Fransson, T. Larsson, B. Sundén, Modeling of an anode supported solid oxide fuel cell focusing on thermal stresses, International Journal of Hydrogen Energy, 41(33) (2016) 14927-14940.

[35] V.A. Danilov, M.O. Tade, A new technique of estimating anodic and cathodic charge transfer coefficients from SOFC polarization curves, international journal of hydrogen energy, 34(16) (2009) 6876-6881.

[36] J. Gazzarri, O. Kesler, Non-destructive delamination detection in solid oxide fuel cells, Journal of power sources, 167(2) (2007) 430-441.

[37] G.F. Naterer, C. Tokarz, J. Avsec, Fuel cell entropy production with ohmic heating and diffusive polarization, International journal of heat and mass transfer, 49(15-16) (2006) 2673-2683.

[38] D. Saebea, S. Authayanun, Y. Patcharavorachot, N. Chatrattanawet, A. Arpornwichanop, Electrochemical performance assessment of low-temperature solid oxide fuel cell with YSZ-based and SDC-based electrolytes, International Journal of Hydrogen Energy, 43(2) (2018) 921-931.

[39] F. Qiang, K. Sun, N. Zhang, X. Zhu, S. Le, D. Zhou, Characterization of electrical properties of GDC doped A-site deficient LSCF based composite cathode using impedance spectroscopy, Journal of power sources, 168(2) (2007) 338-345.

[40] O.A. Marina, L.R. Pederson, M.C. Williams, G.W. Coffey, K.D. Meinhardt, C.D. Nguyen, E.C. Thomsen, Electrode performance in reversible solid oxide fuel cells, Journal of the Electrochemical Society, 154(5) (2007) B452.

[41] K. Miyoshi, T. Miyamae, H. Iwai, M. Saito, M. Kishimoto, H. Yoshida, Exchange current model for (La0. 8Sr0. 2) 0.95 MnO3 (LSM) porous cathode for solid oxide fuel cells, Journal of Power Sources, 315 (2016) 63-69.

[42] A.V. Akkaya, Electrochemical model for performance analysis of a tubular SOFC, International Journal of Energy Research, 31(1) (2007) 79-98.

[43] K.L. Christman, M.K. Jensen, Solid oxide fuel cell performance with cross-flow roughness, Journal of Electrochemical Energy Conversion and Storage, 8(2) (2011) 024501.

HOW TO CITE THIS ARTICLE

M. Taghilou, V. Barati, Enhancing Thermo-Electrical Performance of Solid Oxide Fuel Cells through Multi-Channel Cooling System Analysis, AUT J. Mech Eng., 10(2) (2026) 179-198.

DOI: 10.22060/ajme.2025.23880.6164